Journal of Magnetic Resonance 203 (2010) 294–304

Contents lists available at ScienceDirect

Journal of Magnetic Resonance

journal homepage: www.elsevier.com/locate/jmr

Practical considerations for the design of sparse-spokes pulses

Marcin Jankiewicz [a,*], Huairen Zeng [a], Jason E. Moore [a], Adam W. Anderson [a,b], Malcolm J. Avison [a], E. Brian Welch [a,c], John C. Gore [a,b]

[a] Vanderbilt University Institute of Imaging Science, Vanderbilt University, 1161 21st Ave. South, Nashville, TN 37232, USA
[b] Department of Biomedical Engineering, Vanderbilt University, Nashville, 5824 Stevenson Center, Nashville, TN 37235, USA
[c] Philips Healthcare, MR Clinical Science, Cleveland, OH, USA

ARTICLE INFO

Article history:
Received 8 September 2009
Revised 25 January 2010
Available online 4 February 2010

Keywords:
slice-selective excitation
RF inhomogeneneity mitigation
Sparse-spokes pulse
Ultra-high field MRI
RF pulse design

ABSTRACT

Sparse-spokes pulses are 2D slice-selective pulses that effectively mitigate inhomogeneities in the transmitted RF field and reduce unwanted RF artifacts in MR images. Here we consider the practical design of such pulses for high-field MRI and demonstrate limitations of the technique. We analyze the performance of pulses considering input noise as well as other effects such as saturation and T_2^* relaxation. We discuss in detail the correspondence between the reduction of RF inhomogeneities and the fidelity of the input parameters, such as the transmit B_1^+ field map and combined phase of the main B_0 field and eddy-currents. Results include simulations, utilizing 7 T field maps acquired in phantoms and in-vivo, as well as in-vivo experiments. The necessary performance of system hardware components to achieve significant improvements is described.

1. Introduction

Ultra-high field human magnetic resonance imaging must overcome several technical challenges to be successful. In particular, inhomogenous RF fields arise when the wavelengths of the transmitted RF pulses are comparable to the size of the imaged anatomy [1] and these give rise to various image artifacts and limit the performance of many pulse sequences. However, variations of the RF field can be reduced by the use of slice-selective, tailored 2D pulses optimized for the desired excitation profile [2]. Such pulses approximate the exact modulation pattern necessary to create a homogenous excitation by propagating through a finite set of points in the excitation k-space. To make the pulse length as short as possible, the number of sampled k-space points is kept to a minimum. This sparse-spokes pulse consists of a train of amplitude and phase modulated sub-pulses executed at different locations in the excitation k-space, so transverse gradients G_x and G_y are needed in addition to the slice selective G_z gradient. Pulses are tailored for a specific inhomogenous transmit B_1^+ field and a corresponding total phase map, comprised of ΔB_0 field and eddy-current phase ϕ_{eddy} contributions.

The positions of the points in k-space and thus the transverse gradients together with the RF amplitudes and phases of the corresponding sub-pulses are determined by an optimization problem that minimizes the difference between the simulated and target excitation profiles. The details of the design as well as necessary theoretical background are summarized in Section 2. Recently, several designs of sparse-spokes pulses with experimental verification have been presented [3], including the use of parallel RF arrays [4,5]. We acknowledge the advantage of the parallel-transmit methods over the single channel solution presented here. However, since parallel transmit is not universally available on 7 T systems, we believe that studies with a single transmit channel are still valuable. Moreover, the practical limitations and implementation challenges have not been discussed in the literature. Here we describe step by step the pulse design process, identify possible sources of problems like imperfections in B_1^+ mapping, unstable measurements of total phase and more generally noisy RF inputs. In addition, the duration of sparse-spokes pulses executed on a single transmit channel are in the range of 5–15 ms, and thus may be affected by T_2^* relaxation and saturation effects. The main aim of this work is to understand the origin of the limitations on the performance of the sparse-spokes solution as well as to present solutions to some of the problems described above. First we present background material needed to understand the theory of sparse-spokes. In the methods and corresponding results sections we offer technical details of our experimental implementation and numerical simulations. We review the B_1^+ mapping technique and describe the method that we use to test the susceptibility of the B_1^+ map to high spatial-frequency noise as well as discuss the influence of this noise on the performance of sparse-spokes pulses. In the next section we describe in detail the technique used to

* Corresponding author.
E-mail addresses: m.jankiewicz@vanderbilt.edu (M. Jankiewicz), h.zeng@vanderbilt.edu (H. Zeng), jay.moore@vanderbilt.edu (J.E. Moore), adam.anderson@vanderbilt.edu (A.W. Anderson), calum.avison@vanderbilt.edu (M.J. Avison), brian.welch@philips.com (E.B. Welch), john.gore@vanderbilt.edu (J.C. Gore).

1090-7807/$ - see front matter © 2010 Elsevier Inc. All rights reserved.
doi:10.1016/j.jmr.2010.01.012

measure total phase and its problems. We then analyze the influence of errors in the input RF amplitude and phase. In later sections we analyze the pulse performance change in the presence of T_2^* relaxation, as well as the influence of T_2^* relaxation and saturation effects on the RF amplitudes of the sparse-spokes sub-pulses. Finally, we show a modification of the optimization problem that utilizes multiple flip-angle maps and addresses some of the related issues.

2. Theory

The image intensity, SI, generated using a gradient-recalled echo (GRE) sequence, can be expressed as follows

$$\mathrm{SI}(\mathbf{r}) = \rho(\mathbf{r}) \cdot |(\widehat{B}_1^-)^*(\mathbf{r})| \cdot \sin(\alpha(\mathbf{r})) \frac{1 - e^{-TR/T_1(\mathbf{r})}}{1 - e^{-TR/T_1(\mathbf{r})}\cos(\alpha(\mathbf{r}))} \tag{1}$$

with proton density $\rho(\mathbf{r})$ and relaxation time $T_1(\mathbf{r})$, at position $\mathbf{r}(x,y)$, within a given slice. Here,

$$\alpha(\mathbf{r}) = \gamma \cdot |\widehat{B}_1^+(\mathbf{r})| \cdot W(\mathbf{r}) \tag{2}$$

is a flip-angle map in radians, γ is the gyromagnetic ratio for hydrogen, $|\widehat{B}_1^+(\mathbf{r})|$ is the inhomogenous transmission RF profile, and $W(\mathbf{r})$ represents a spatial excitation profile. The flip-angle map is inhomogenous because the transmission profile is inhomogenous due to standing wave/dielectric effects. The $(\widehat{B}_1^-)^*$ field represents the receptivity of the receiving coil to the nuclear magnetization. Hence $\rho \cdot (\widehat{B}_1^-)^*$ is a proton-density-weighted reception profile. Using a sufficiently long repetition time (TR) one can eliminate the dependence of $\mathrm{SI}(\mathbf{r})$ on $T_1(\mathbf{r})$ giving [6]:

$$\mathrm{SI}(\mathbf{r}) = \rho(\mathbf{r}) \cdot |(\widehat{B}_1^-)^*(\mathbf{r})| \cdot \sin(\alpha(\mathbf{r})) \tag{3}$$

The flip-angle map defined in Eq. (2) can be mitigated by either RF shimming [9] of the transmit profile, or by tailoring the excitation profile $W(\mathbf{r})$ to excite an inverse of the transmit profile up to a constant α_{nom} such that

$$\alpha(\mathbf{r}) = \alpha_{nom} \tag{4}$$

α_{nom} is the nominal flip-angle defined *a priori* in the experiment. We define an ideal excitation profile:

$$W_{ideal}(\mathbf{r}) = \alpha_{nom} \cdot \gamma^{-1} \cdot |\widehat{B}_1^+(\mathbf{r})|^{-1} \tag{5}$$

where $|\widehat{B}_1^+(\mathbf{r})|^{-1}$ means the point-wise inverse of the transmission profile. In order to design such an ideal excitation profile W_{ideal}, we would need to sample excitation k-space with an infinite number of points. In order to create a practical solution, W_{actual}, the ideal excitation must be approximated. The excitation profile can be tailored through the optimization of RF complex amplitudes and the excitation gradients. The explicit form of the excitation profile, assuming that we neglect T_1 and T_2 relaxation effects [7,8], is given by

$$W(\mathbf{r})_{actual} = \int_0^T \hat{b}(t) e^{2\pi i \mathbf{k}(t)\cdot\mathbf{r}} e^{i\gamma\Delta B_0(\mathbf{r})(t-T)} e^{i\phi_{eddy}} dt \tag{6}$$

with the RF pulse $\hat{b}(t) = A(t)e^{i\phi_{RF}(t)}$; $\mathbf{k}(t)$ the trajectory in the excitation k-space, and T being the pulse length. This form of excitation profile $W(\mathbf{r})$ assumes a small-tip angle approximation. The approximated excitation profile W_{actual} after discretization of Eq. (6) can be written as a sum

$$W_{actual} = \sum_{j=1}^{M} A_j \Phi_{RF}^j \Phi_G^j \Phi_{\widehat{B}_0}^j \Phi_{eddy}^j \Delta_t^j \tag{7}$$

where M corresponds to number of spokes (i.e., sub-pulses), A_j is the amplitude of jth spoke, $\Phi_{RF}^j = \exp(i\phi_{RF}^j)$, $\Phi_G^j = \exp(2\pi i \mathbf{k}_j \cdot \mathbf{r})$, $\mathbf{k}_j = (k_x^j, k_y^j)$ is the position of the jth spoke in excitation k-space, related to the phase selective (transverse) gradients by $\mathbf{k}_j(t) = -\gamma \cdot \int_t^T \mathbf{G}_j(\xi)d\xi$; $\Phi_{B_0} = \exp[i\gamma\Delta B_0(\mathbf{r})(t_j - T)]$ is the phase accrual due to the inhomogeneity of the main field B_0 and $\Phi_{eddy}^j = \exp(\pm i\phi_{eddy}^j)$ is the phase due to eddy currents, with +/− for an odd/even spoke (the combined phase due to Φ_{B_0} and Φ_{eddy} is what we later call total phase); $\Delta_t^j = T/M$ is the spoke duration, i.e. period of time needed to execute the RF sub-pulse and move to another location in the excitation k-space where the next sub-pulse will be executed. We point out that in discrete form of the excitation profile, given by Eq. (7) a small tip-angle condition is realized by each sub-pulse. Given the definitions, a spokes sequence for given B_1^+ and total phase maps is determined by numerical solution of the minimization problem

$$\underset{(A_j,\phi_{RF}^j,\mathbf{k}_j)}{argmin} |W_{ideal} - W_{actual}| \tag{8}$$

where $A_j,\ \phi_{RF}^j,\ k_x^j,\ k_y^j$ are the free parameters, subject to constrained optimization.

3. Methods

3.1. Imaging protocols

Three healthy volunteers 25–35 years old, all males, were recruited from the community to serve as imaging subjects for this study. All protocols were approved by the local Institutional Review Board (IRB). A 17 cm diameter spherical dielectric phantom, containing realistic concentrations of common brain metabolites and doped with paramagnetic agent to reduce T_1 ($T_1 \sim 300\,ms$), was used to illustrate issues related to total phase instability. Experiments were conducted on a 7 T Philips Achieva whole body scanner (Philips Healthcare, Cleveland, OH) based on a Magnex 90 cm magnet and a single-channel, volume quadrature transmit/receive head coil from Nova Medical (Wilmington, MA) with a 29 cm inner diameter.

All data in this study were collected with a 2D gradient-recalled echo sequence with a Gaussian-sinc excitation pulse, 80 × 80 matrix, FOV = 24 × 24cm, voxel resolution = 3 × 3 × 5 mm, TE = 8 ms. First, a map of the transmitted RF field B_1^+ was acquired. For B_1^+ mapping, a series of 11 images with TR = 5000 ms and flip-angles ranging from 10° to 210° in equal 20° increments, was subject to a 2 parameter fit. A combination of relatively long TR and low-FA excitations (less than 20°) proton-density-weighted images were obtained for a final comparison between uncorrected and corrected images. Total duration of the scans necessary for B_1^+ mapping was 25 min. The dynamic scans for the total phase map were acquired with TR = 2000 ms with scan duration varying from 22 min for 25 spokes to 9 min for 10 spokes; in all cases an EPI factor of 3 was used. Since most of the pulse time is spent traversing the k_z direction, the duration of the RF pulse is strictly limited by the maximum allowed gradient and the slew rate of the slice selective gradient G_z. Hardware limitations of a maximum RF amplitude of 15 μT, a maximum gradient amplitude of 33 mT/m and maximum slew rate of 166 T/m/s were incorporated directly into the optimization routines. The sub-pulse amplitudes and phases as well as the transverse and slice selective gradients were passed to the scanner in waveforms in which we specify values at time steps equal to the scanner's dwell time (6.4 μs). In all experiments, i.e. phantom and in-vivo, we fixed the duration of the RF sub-pulses/slice selective gradients to 88 dwell times, and transverse gradients to 16 dwell times. Because of current memory limitations, which limits each waveform to 3000 points and issues related to long pulse durations, we limit ourselves to pulses with 25 spokes, with 2600 dwell time points per waveform, leaving free 400 points for refocusing gradients. A sample pulse

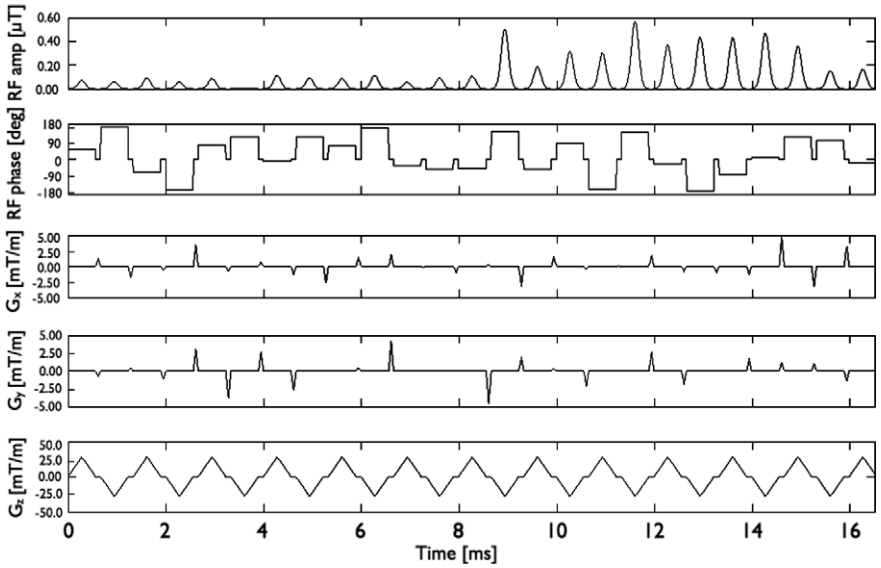

Fig. 1. The amplitudes and phases of RF sub-pulses together with transverse G_x G_y and slice-selective G_z gradients. The pulse consists of $n_{spokes} = 25$ sub-pulses, each corresponding to a different spoke in transverse excitation k-space.

consisting of 25 spokes is presented together with corresponding gradient waveforms in Fig. 1.

In order to handle the minimization problem given by Eq. (8) we used a standard Matlab (The Mathworks, Natick, MA, USA) constrained nonlinear multivariable minimization routine `fmincon`, with the active-set (linear) algorithm that computes a quasi-Newton approximation to the Hessian of the Lagrangian defined by Eq. (8). All the hardware restrictions, i.e., maximum RF amplitude, gradient amplitude and slew-rate, were used to constrain the model. For all the fitting problems we utilized Matlab's unconstrained search function `fminsearch` based on the simplex method. Matlab was also used to calculate the gradient as well as RF waveforms. In all of our experiments a 10° spokes pulse was used. However, depending on the length of the designed pulse (i.e. number of sub-pulses in the sequence) the maximum value of the flip-angle that can be excited without violating the small flip-angle approximation varies. In our design we did not constrain the maximal flip-angle in the cost function that was optimized. Hence, the performance of the pulse will depend on the distribution of RF amplitude among the spokes. As the number of spokes grows, so does the variation of sub-pulse amplitudes. For this reason, the small flip-angle approximation holds for 10 spokes at 60° but only up to 30° for 25 spokes.

3.2. Pulse performance and B_1 mapping

The performance of a spokes pulse is sensitive to the accuracy of the input flip-angle map. After testing several methods [10–14], we decided for development purposes to use a method involving the fitting of Eq. (3) in a similar way to the one presented in [13]. The results of the fitting method are represented in Fig. 2. Throughout the paper a B_1^+ map will be represented by the ratio of measured to the nominal flip-angle α_{nom}.

There is a tradeoff between number of spokes, M, and the performance of a given pulse. The more sub-pulses there are, the higher the potential is to correct high spatial frequency details. Correction of these details may seem advisable, but there is a drawback to this approach. These high spatial-frequency details are vulnerable to errors in estimates of the B_1^+ field.[1] Therefore, correction of these details should not be a priority in practice. The susceptibility of the M-spokes pulse to high spatial-frequency variations was tested. First, a set of N noisy B_1^+ maps was generated. Each new map is generated by introducing noise into the real ($\Re_j$) and imaginary ($\Im_j$) parts of each image in the original GRE series. The amplitude of high spatial frequency gaussian noise distinguishes each B_1^+ map, viz.

$$\epsilon_j = \kappa \cdot 1/SNR_j \cdot \max(GRE_j) \cdot \texttt{randn}, \tag{9}$$

where a constant κ sets a magnitude of the noise and varies from 0.1 to 2.0 in 0.1 increments, resulting in $N = 20$ noisy maps overall; SNR_j is the mean signal-to-noise ratio of the images from the GRE series used to generate the ideal B_1^+ map; $\max(GRE_j)$ is a maximum intensity of either real or imaginary part of GRE_j image; `randn` is a normally distributed Gaussian number. Index j numbers GRE images in the series. The noise in this form is then added to the real ($\Re_j$) and imaginary ($\Im_j$) parts of each GRE image, i.e.:

$$GRE_j^{noisy} = \left[\left(\Re_j + \epsilon_j^{\Re}\right)^2 + \left[\Im_j + \epsilon_j^{\Im}\right)^2\right]^{\frac{1}{2}}, \quad j = 1, \ldots, 11 \tag{10}$$

Finally, a B_1^+ map was calculated from a set of GRE^{noisy} images. An example of a new fitted noisy map is presented in Fig. 3b. It is important to observe that the low signal-to-noise-ratio regions are affected measurably by the noise. Therefore, these regions are expected to be primarily affected in the B_1^+ field map. For each noisy map in a set, a sparse-spoke pulse with M sub-pulses was generated. As a result, N corrected flip-angle maps FA_i^M were obtained. Next, for a given value of M, the standard deviation was calculated

$$\sigma_M = \frac{1}{N}\left[\sum_{i=1}^{N}\left(\mathrm{id} - FA_i^M\right)^2\right]^{\frac{1}{2}}, \tag{11}$$

where id is ideally corrected flip-angle map (nominal/measured flip-angle), corresponding to a binary mask of the FOV under consideration. The entire procedure was repeated for $M = 1, \ldots, 25$. The block diagram presented in Fig. 4 summarizes this entire noise simulation procedure. Comparison of calculated σ_M values vs. M allows for selecting M on the basis of the robustness of the pulse to variations in the B_1^+ measurement. The evaluation scheme shown in Fig. 4, evaluates the root mean square difference between the cor-

[1] To simplify the notation, starting from this section, the hat and absolute value of $|\widehat{B}_1^+|$ will be dropped.

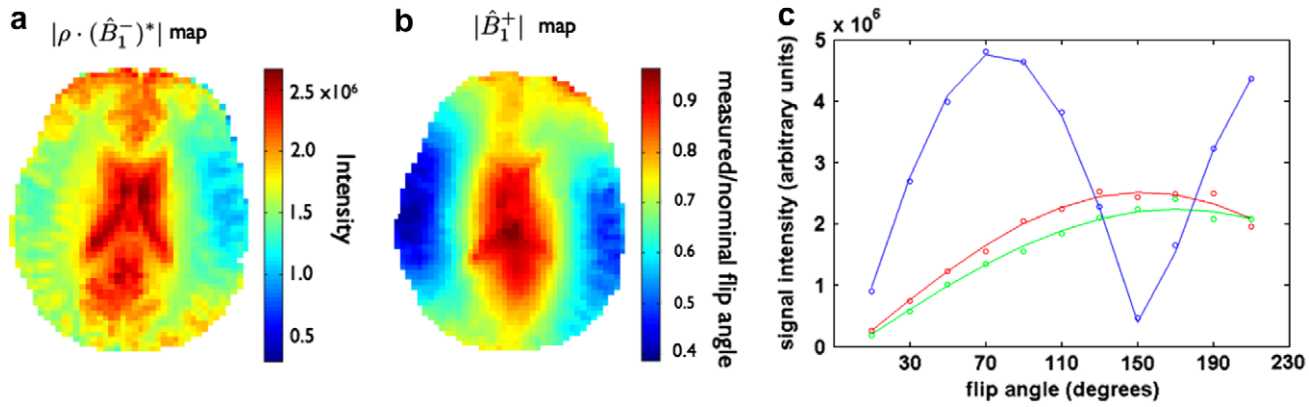

Fig. 2. B_1 mapping using a two-parameter fit of a series of GRE images with a range of nominal flip-angles from 10° to 210° with increments of 20°. (a) A map of proton-density-weighted reception profile $\rho \cdot (\hat{B}_1^-)^*$. (b) The $\hat{B}_1^+$ intensity represents the fraction of nominal $\hat{B}_1^+$ amplitude at each point in space. (c) GRE intensity values (circles) and fitted curves (solid lines) for three representative voxels.

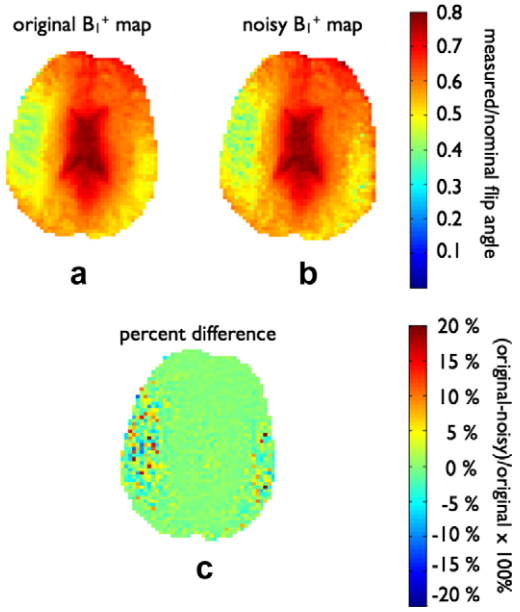

Fig. 3. Original (a) and noisy (b) B_1^+ maps. A noisy map is generated using the procedure explained in the text. A percent difference map (c) shows that low signal-to noise-ratio regions are affected most by the noise.

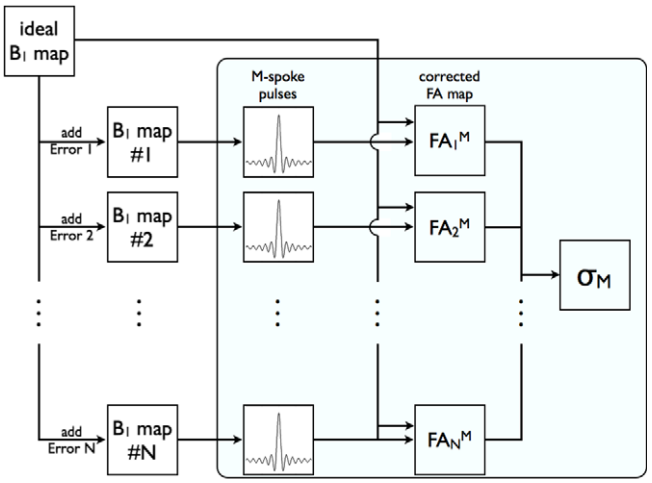

Fig. 4. This block diagram summarizes the procedure for determining the sensitivity of sequences with M spokes to variations in B_1^+ maps. Shaded part of the diagram is repeated for each value of M.

rected and ideal flip-angle maps due to image noise (Eq. 11). This is sensitive to both bias and variations in the estimated B_1^+ maps.

3.3. Total phase instability

The excitation profile is sensitive not only to the fluctuations in the B_0 field but also to eddy current induced changes in the gradient fields, which in turn affect the overall phase of the magnetization. An accurate map of the total phase due to B_0 inhomogeneities and eddy currents is therefore a necessary input for designing a spokes pulse that will perform as anticipated.

Total phase maps are measured by executing the entire oscillating G_z waveform of the spokes sequence (Fig. 1), but turning on only one of the RF sub-pulses at a time. Although the amplitudes and phases of the n_{spokes} RF pulses in a spokes sequence generally vary, all RF sub-pulses used for the purposes of the total phase measurements are identical. The magnitude and phase of the magnetization are then recorded via a GRE acquisition, and the process is repeated for the next sub-pulse. For each excitation, the G_x and G_y waveforms are turned off and the phase of the given sub-pulse is set to 0. Thus, the phase of the magnetization for each acquisition reflects the phase due only to ΔB_0 and eddy currents arising from the RF field and the G_z waveform. Eddy currents from the low-amplitude G_x and G_y waveforms are therefore assumed insignificant in comparison. The extra phase due to ΔB_0 and eddy currents (Fig. 5) measured via this technique can then be incorporated into the optimization of the spokes sequence. This step is crucial for generating a spokes pulse for which simulated and experimental data agree.

Besides B_1 mapping, one of the main implementation challenges for the sparse-spokes pulse design is the instability of the total phase during the period of time ΔT, between measurement of the phase set and the execution of the designed pulse. As mentioned in Section 3.1, the acquisition times for the total phase maps can be very long (up to 22 min for 25 spokes) hence it is important to check the temporal stability of total phase measurements. The set of total phase measurements was re-acquired after $\Delta T = 16$ min. ΔT is long enough to observe magnet drift and thermal fluctuations in the gradient coils, as well as other experimental imperfections of the hardware/design that could affect our measurements. For the second scan the same scanner preparation was used (i.e., the same RF drive scale, B_0 shim set, etc.) as the earlier series. To make the effects of unstable total phase measurement more obvious this experiment was performed

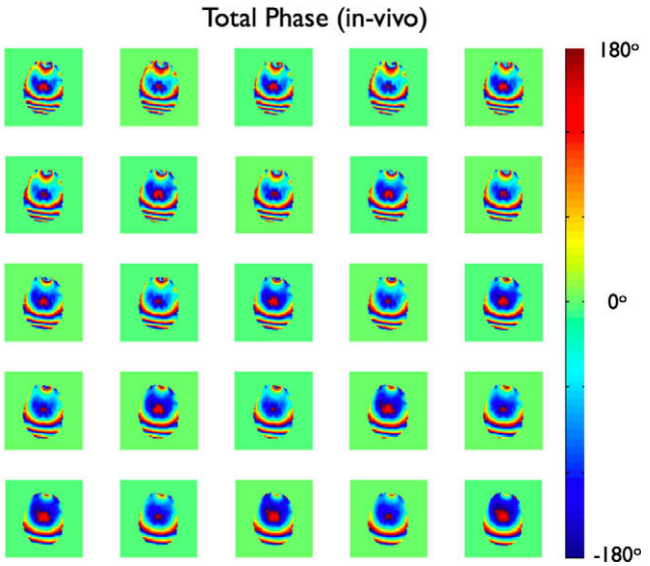

Fig. 5. The total phase due to ΔB_0 and eddy currents as measured for each of the $n_{spokes} = 25$ sub-pulses of the spokes sequence. Colors represent phases in degrees from -180° to $+180^\circ$. Spoke 1 is shown in the upper left corner and spoke number increases to the right. (For interpretation of the references to color in this figure legend, the reader is referred to the web version of this paper.)

on the central slice of a homogenous spherical phantom. First, total phase was measured (Fig. 6b) and was used as a reference, and another measurement was performed 16 min later. In order to quantify the difference between the two sets of measurements, the relative total phase maps were calculated (Fig. 6b). The maps were obtained by subtracting the first phase map from each of the subsequent measurements of that series. Finally, the difference in relative total phase measurements was calculated resulting in a measure of temporal phase instability as a function of sub-pulse position number.

3.4. Simulated RF amplitude and phase instability

To understand how sensitive the sparse-spokes design is to phase instabilities, we have simulated the effect of phase errors on the performance of the $M = 25$ sparse-spokes pulses. Although, the 25 spokes pulse is likely too long (16.6 ms) for practical use, we believe that it is useful to analyze the level of performance in this hypothetical limit. Ideally, this pulse should correct the original flip-angle map from a mean $0.68 \pm 19\%$ to $1.00 \pm 3\%$ (Fig. 7a). For example, Fig. 7(c) shows what would happen if the information about the total phases were removed from the optimization input. This simulation shows that even small variations of the total phase maps can ruin the performance of the pulse. Using this pulse, we generated an array of noise values and added it to the RF amplitudes and phases. Adjusting RF amplitude and phase is equivalent to introducing error in the total magnitude and phase of the magnetization. In this way, we can check what would be the effect of RF errors on the percent error of the flip-angle distribution. The entries in the noise array were normally distributed random numbers with mean value set to zero. The RF amplitude noise was then increased from 0% to 10% of the maximum of the initial RF amplitude. The noise of RF phase was increased from 0° to 20°. The values chosen here represent a pessimistic scenario where either RF amplitude, phase or both cannot be set with required precision. It should be understood that the errors tested exceed the range expected in typical experimental conditions. The analysis presented above was then repeated for the pulses with 5, 10, 15 and 20 spokes. For each case a percent error difference was calculated as a normalized difference between the inhomogeneity affected by noise and original inhomogeneity. In this context, inhomogeneity is understood to be calculated as a standard deviation from a mean of the flip-angle distribution normalized by the value of the mean of this distribution (the coefficient of variation of the flip-angle). To illustrate the effect of phase noise in the input, the original flip-angle map was corrected with the initial pulse, but this time RF phase noise (maximum amplitude set to 20°) was added to the original phase. The simulated correction can be seen in Fig. 7b.

3.5. Simulated T_2^* effects

In this section, the relevance of T_2^* relaxation on the performance of the sparse-spokes pulses will be quantitatively addressed. As described in the previous sections, the design of the RF pulses presented here does not take into consideration any relaxation effects, i.e. the pulses are designed in the limit of $T_2^* \to \infty$. However, taking into account the fact that the sparse spokes pulses can be long (up to 16 ms for $n_{spokes} = 25$ and 5 mm

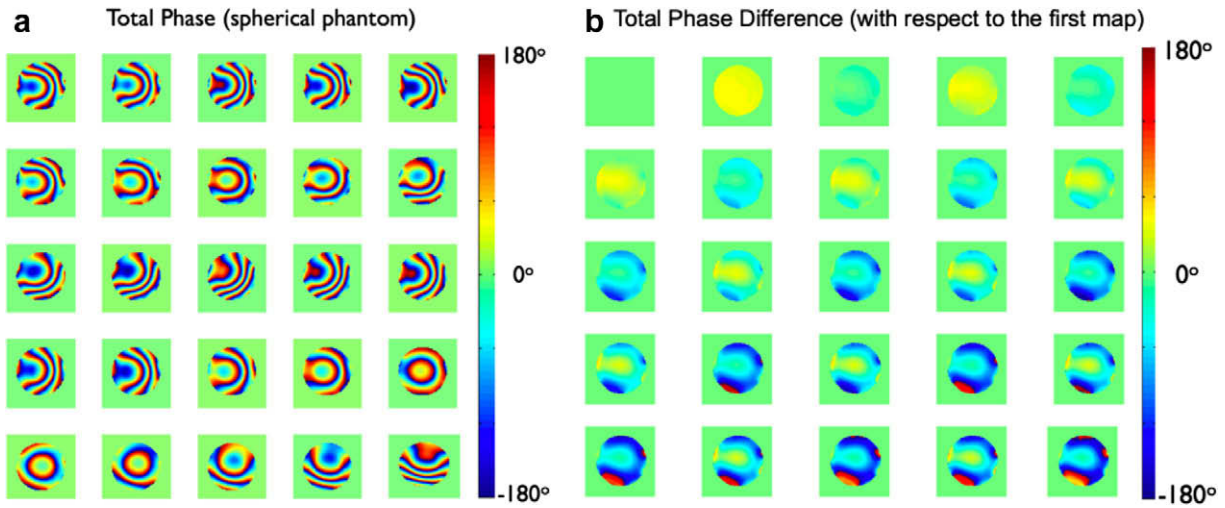

Fig. 6. (a) The total phase as measured for each of the 25 sub-pulses of the spokes sequence. Colors represent phases in degrees from -180° to $+180^\circ$. (b) The relative total phase as measured for each of the 25 sub-pulses of the spokes sequence. The first phase map from the series has been subtracted from each of the subsequent measurements. Colors represent relative phases in degrees from -180° to $+180^\circ$. (For interpretation of the references to color in this figure legend, the reader is referred to the web version of this paper.)

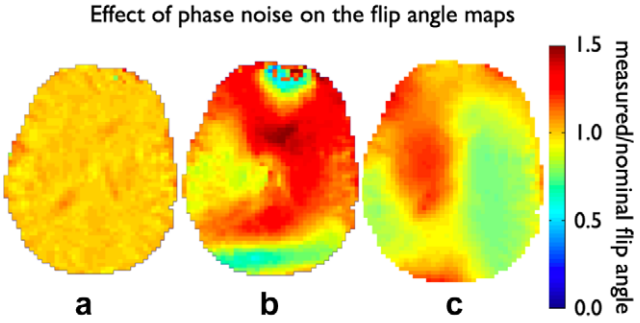

Fig. 7. Simulated flip-angle maps, corrected with (a) original sparse spoke pulse ($n_{spokes} = 25$), leading to mean 1.00 and 3% percent error; (b) a pulse with a noisy RF phase with mean 1.10 and a higher 18% percent error. Another pulse with 25 spokes designed without total phase map input, was executed in a presence of total phase (c), leading to performance drop from $1.00 \pm 3\%$ to $0.95 \pm 15\%$. Clearly, a set of total phase measurements is necessary for efficient mitigation.

slice thickness) it seems warranted to check if relaxation effects will change the performance of the pulses. We tested these effects by executing M-spokes pulses of given length in a system of Bloch equations that includes the T_2^* relaxation term. Pulse length was varied to quantify how the susceptibility to T_2^* varies as a function pulse length. In the simulations, a mean and a standard deviation of the flip-angle map, degraded by the relaxation effect were calculated. These two parameters objectively characterize the performance of a pulse. For simplicity, we worked with a uniform T_2^* mask, i.e. a single value of T_2^* was assigned to the imaged slice. We repeated the simulations for a range of values of T_2^* starting from 5 ms and ending at 100 ms in 1 ms increments.

3.6. Adjustment of RF amplitudes of individual spokes due to saturation and T_2^* effects

Saturation and T_2^* relaxation effects on the amplitudes of the RF sub-pulses were analyzed, as they may cause notable discrepancies between simulated and experimental flip-angle maps if not incorporated into the pulse design. The amplitude of each sub-pulse has to be adjusted to accommodate both effects. To illustrate this issue, a long pulse, consisting of 25 sub-pulses, was considered. The amount by which the RF amplitude should be adjusted can be found from the intensity of the images used to find total phase maps after each spoke, described in Section 3.3. Again, the entire G_z waveform is executed with only one sub-pulse turned on at each time. Similarly, amplitudes of all sub-pulses are set to be identical and the phases together with transverse gradients G_x and G_y are set to zero. With this setup, one can compare the intensities of each of the images in the dynamic GRE series. We also introduce the normalized averaged intensity (NAI), which is the average value of intensity over the image and normalized to the average of the intensity measured after the first sub-pulse. The values of NAI can be used to find the relations between the relative RF amplitudes of the sub-pulses.

3.7. Modification of the optimization problem

The original optimization problem introduced in Eq. (8) can be modified to enable design of a pulse that could be effective on multiple subjects. Because of the long time needed for acquisition of B_1^+ and total phase maps, this approach could potentially have significant practical advantages. Instead of a single ideal excitation profile W_{ideal}, one can run the optimization on a set of N different profiles W^i_{ideal}, i.e. the condition in Eq. (8) will be replaced by:

$$\underset{(A_j,\phi^j_{RF},k_j)}{argmin} \sum_i^N |W^i_{ideal} - W_{actual}| \tag{12}$$

We run the optimization on a set with two different flip-angle human brain maps and total-phase maps. The resulting pulse was then executed on a new (different) set of flip-angle and total phase maps. We checked the performance drop of the resulting pulse.

4. Results

4.1. Pulse performance and B_1 mapping

A plot of σ_M vs. M is presented in Fig. 8. For comparison, the simulations were performed on a human head and a spherical phantom. In both cases, pulses with only 10 spokes generate results very comparable to those of longer pulses. This means that long pulse trains (with up to 25 spokes) are not more effective in correcting high spatial frequency details of the flip-angle maps. This reflects the fact that one is limited by the gradient strength and slew-rate in our design. Hence, the effective area of the excitation k-space covered by the optimized trajectory is really limited to relatively long wavelength effects, and so even with 25 spokes we won't be able to traverse far from the origin of the excitation k-space. Moreover, because the in-plane variations of B_1^+ are relatively smooth, they can be addressed with a relatively limited number of spokes. Therefore, contamination by high spatial frequencies has little effect on pulse performance, as can be seen in Fig. (9), where the exact and designed excitation patterns were shown. The designed pattern shows no anatomical details.

4.2. Total phase instability

Temporal phase instability as a function of dynamic scan number is presented in Fig. 10a. Ideally, this temporal phase instability would be minimal, i.e. the phase maps should not change over time; however, variations large enough to significantly affect the performance of a spokes sequence were measured. We conclude that total phase variations in the example presented here ($n_{spokes} = 25$) phase deviations are up to $\pm 20^\circ$. Phase errors on this scale significantly degrade sparse-spokes pulse performance. For example, for a pulse executed in the presence of these phase errors, a performance drop was observed from $1.00 \pm 3\%$ to $0.95 \pm 15\%$ (Fig. 7c). In order to minimize these effects, we measured the central frequency of the water proton spectrum f_0 before every dynamic scan (Fig. 10c) and accordingly adjusted the RF

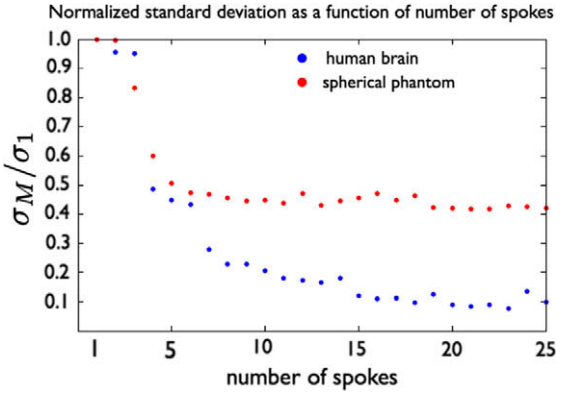

Fig. 8. Normalized standard deviation of flip-angle calculated based on $N = 20$ noisy maps, corrected with M-pulses versus number of spokes M. Blue (red) dots represent human brain (phantom) data. (For interpretation of the references to color in this figure legend, the reader is referred to the web version of this paper.)

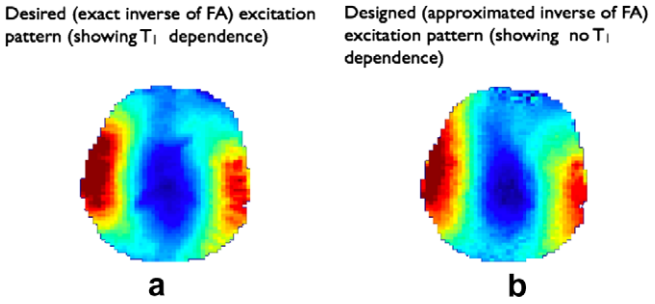

Fig. 9. Excitation pattern: (a) desired-point-wise inverse of the flip-angle map; (b) designed-approximated by the optimization given by Eq. (8).

transmission frequency. The resulting modification shows an improvement, as can be seen in Fig. 10b. This modification significantly improves agreement between phase difference measurements taken 16 min apart (compare Fig. 10a and b); however, there remains a significant mismatch ($\pm 10^{\circ}$) in measured phase difference at least for some of the 25 scans in the dynamic series. These phase errors, possibly caused by coarseness of the f_0 measurement, could be a major limitation to a sparse-spokes implementation. These variations are small; however, the accumulated phase over 16 min of mapping leads to significant error (Fig. 10). To test this hypothesis we checked how the phase error influences the behavior of the sparse-spokes pulses.

4.3. Simulated RF amplitude and phase instability

Ten percent uncertainties in the RF amplitude or 20° errors in the RF phase of sub-pulses creates noticeable deviations in the desired corrected flip-angle map. The results of the simulations are represented in Fig. (11) where one can see how the percent error of the flip-angle maps behaves as a function of RF error. The results for 5, 10, 15, 20 and 25 spokes-pulses are represented on Fig. (12). To a reasonable approximation, percent difference depends linearly on the RF phase noise amplitude. The longer the pulse, the higher the slope of the linear dependence between the percent difference and RF phase noise amplitude. Thus, even the longer pulses, that initially perform better, can loose their performance characteristics due to the error induced in RF inputs. We conclude that the pulse with $n_{spokes} = 10$ is the only one that improves the homogeneity within the discussed range of the induced RF phase noise (in Fig. 12).

4.4. Simulated T_2^* effects

The mean and normalized standard deviation (percent error) of flip-angle as a function of T_2^* background for the pulses with 5, 10, 15, 20 and 25 sub-pulses are presented in Fig. (13). As can be seen in that figure, in a region of experimentally interesting values of T_2^*, i.e., between 20 ms and 60 ms, only pulses with 5 and 10 spokes show insignificant performance drop in both mean and percent error. At $T_2^* = 30$ ms (an average value for the human brain at 7 T

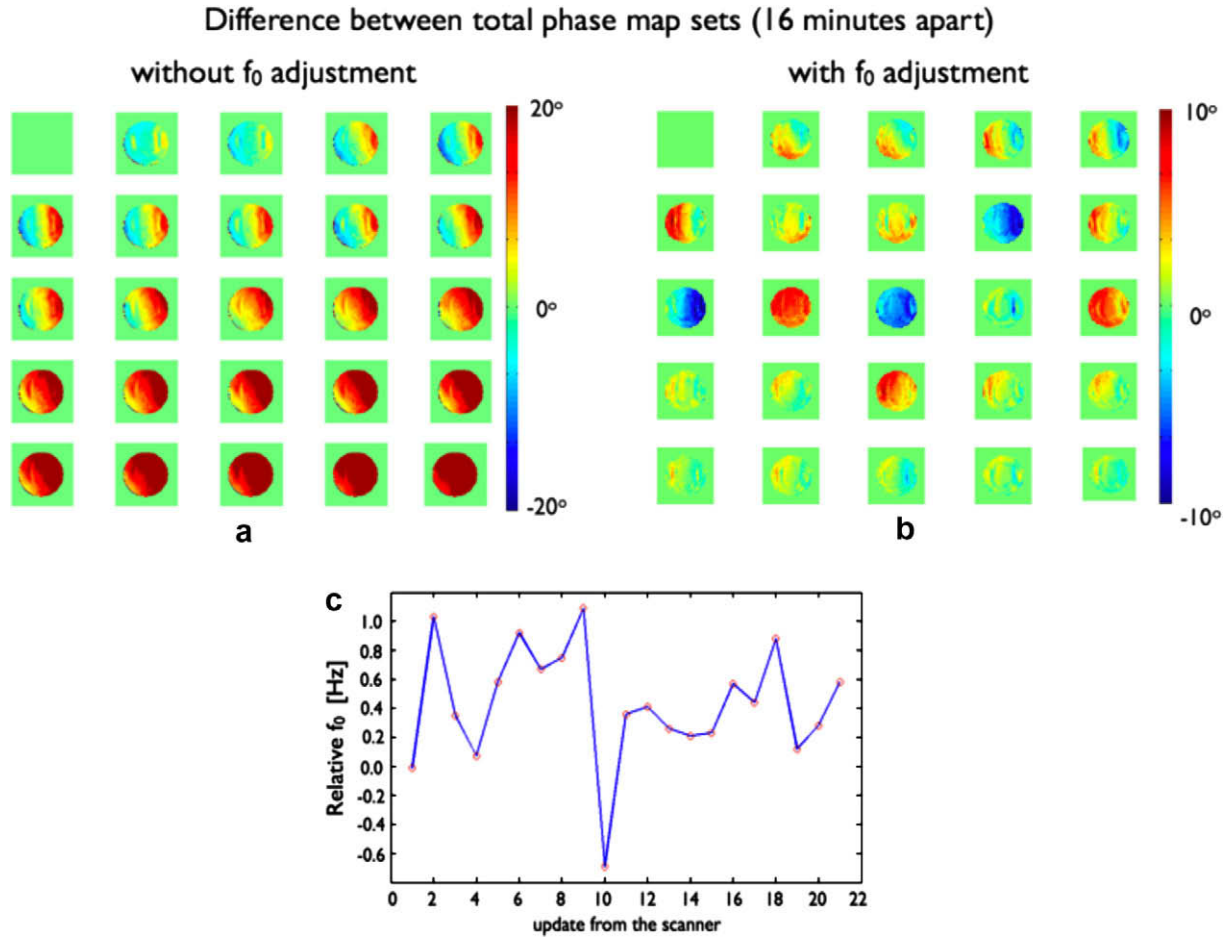

Fig. 10. Phase difference without (a) and with (b) updated f_0 value. Colors represent phase differences in degrees from -20° to 20° and -10° to 10° correspondingly. (c) The Δf_0 shift values updated before every dynamic scan. The values are used in the calculation of the evolution of total phase during the sparse-spokes pulse duration. (For interpretation of the references to color in this figure legend, the reader is referred to the web version of this paper.)

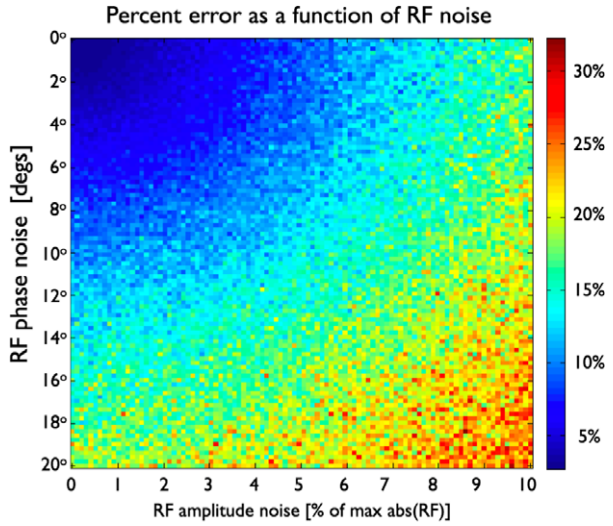

Fig. 11. Percent flip-angle error as a function of RF error. Color bar represents value of the percent error and ranges from 0% to 30%. (For interpretation of the references to color in this figure legend, the reader is referred to the web version of this paper.)

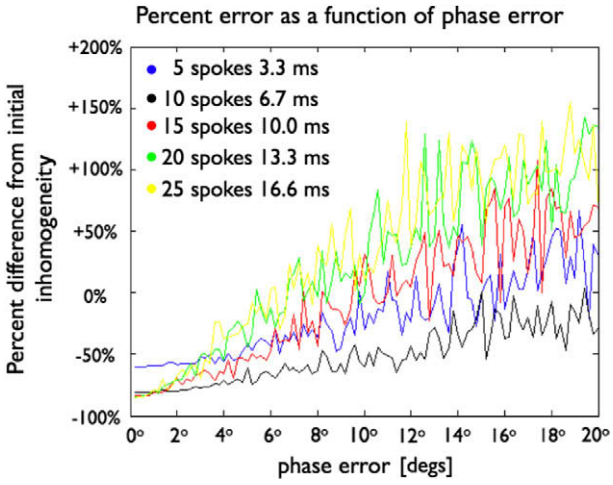

Fig. 12. Percent flip-angle difference from the uncorrected inhomogeneity (here 19%) as a function of phase error, ranging from 0° to 20°, induced through RF phase of a pulse with 5, 10, 15, 20 and 25 spokes. The improvement is achieved when the difference is negative. The RF pulse with 10 spokes is the only pulse that shows improvement over the whole range of induced phase error.

[15]) only these two pulses are immune to the relaxation effects, as can be seen on the percent error plot (Fig. 13b). Moreover, the relative amplitude of spokes of longer pulses makes their behavior unpredictable, as can be seen in the case of pulses with 20 and 25 spokes, where the shorter pulse has a better behavior than the pulse with 25 spokes.

4.5. Adjustment of RF amplitudes of individual spokes due to saturation and T_2^* effects

If there were no saturation or T_2^* decay all NAI values (defined in Section 3.6) should be the same. However, as one can see in Fig. 14, the NAI values after execution of each sub-pulse vary. The decay from the initial value of NAI is a saturation effect (see Section 5). From this experiment, we obtain a series of factors which we use to correct the amplitudes of the sub-pulses. In the example presented in Fig. 14, an amplitude of the second spoke should be corrected by a factor $(0.984)^{-1}$, third spoke by $(0.989)^{-1}$ etc. This simple solution was incorporated in the pulse design in all of the experiments using pulses with $n_{spokes} > 10$. For pulses with fewer than 10 spokes, a deviation of the amplitudes due to the saturation and T_2^* effects is negligible as the effective echo times for spokes are shorter.

4.6. Modification of the optimization problem

To illustrate how the modified optimization condition would work, a pulse with $n_{spokes} = 10$ was generated using two different

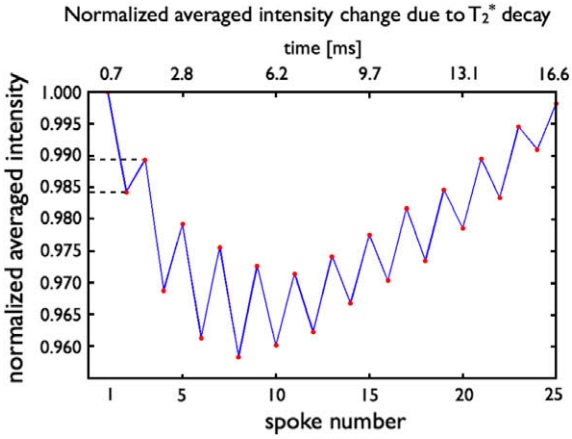

Fig. 14. Normalized averaged intensity (NAI) values for each sub-pulse in a pulse with $M = 25$ spokes. The behavior can be explained by saturation T_2^* effects, and eddy current.

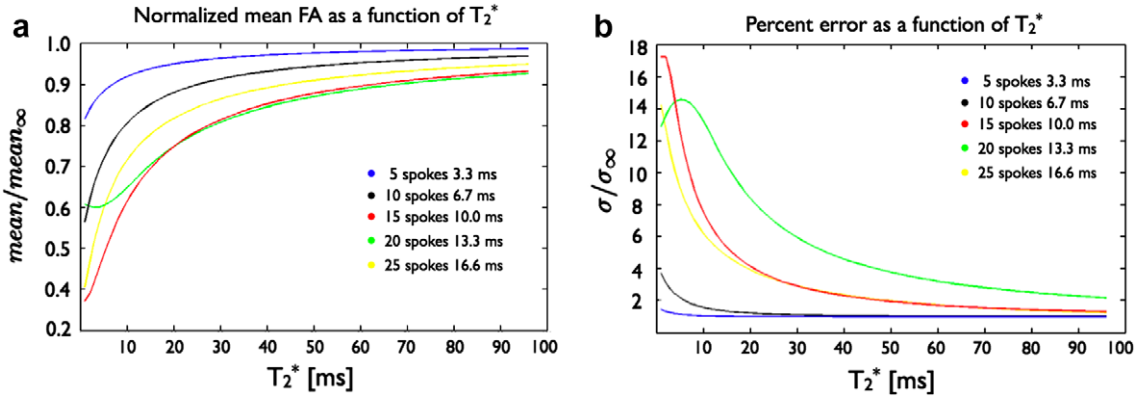

Fig. 13. Mean value (a) and percent error (b) of the flip-angle map and degraded by T_2^* relaxation effects.

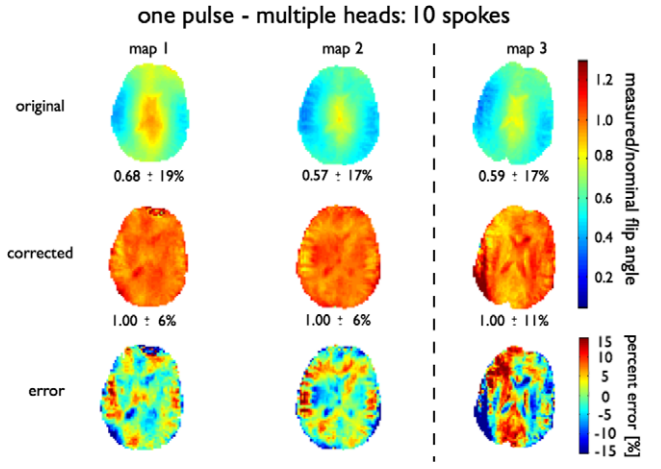

Fig. 15. Simulation of the performance of a 10-spokes pulse generated to mitigate the inhomogeneities of two different B_1^+ maps. First row represents original flip-angle maps for three different subjects. Second row represents simulated corrected maps. The third row shows the percent error maps. The third column shows the data for a map that was not part of the optimization problem.

sets of in-vivo B_1^+ and total phase maps with the modified minimization condition given by Eq. (12). As a result of this modification of the optimization problem, we obtained a pulse and a set of transverse gradients more immune to high spatial-frequency differences in B_1^+ field and total phase maps than the method based on "single map minimization". The overall performance of pulses generated this way is not as high as of pulses generated for a specific slice (Fig. 15). However, this approach represents a convenient way of testing the practical limits of applying one pulse to multiple imaging slices.

5. Discussion and conclusions

In this report, we have discussed practical limitations and implementation challenges of sparse-spokes pulses. We have investigated the design and performance of such excitation schemes for imaging with a human scanner at 7 T. We specifically consider experimental in-vivo results with an optimized 10-spokes pulse (~6.7 ms). Using a standard head coil, the original inhomogenous flip-angle map of a central axial brain slice (presented as a ratio of measured to nominal flip-angles) has a mean of 0.59 with ±17% error, as shown in Fig. 16a. The corrected flip-angle map Fig. 16b shows improvement in the homogeneity. The initial inhomogeneity was reduced by 42%, and the mean flip-angle is now 0.90 of the nominal and the errors are reduced to ±10%. However, there are substantial differences between the predicted and measured corrected maps, i.e. the corrected map has errors up to ±10% of the mean flip-angle in comparison to a simulated corrected map with only ±5%. The differences are primarily in low signal-to-noise ratio regions, and we argue that they are due to imperfections in B_1^+ mapping, its susceptibility to high-spatial frequency noise, as well as unstable total-phase map measurements. Moreover, we acknowledge the fact that if the slice profile of the spokes pulse does not match that of the B_1^+ mapping pulse then the sparse spokes correction may not be complete. However, B_1^+ maps acquired from adjacent 5mm thick slices show little variation, suggesting however that the B_1^+ field varies slowly and smoothly in the through-slice direction and thus does not have a significant effect on the spokes performance. Finally, proton-density-weighted images are shown before Fig. (17a) and after correction Fig. (17b) and show an overall improvement in signal-to-noise ratio.

The major difficulty in the calibration of the sparse-spokes design is the total phase measurement. As can be seen from Fig. 10(a and b), the variations in the phase errors can reach up to ±10°. These devi-

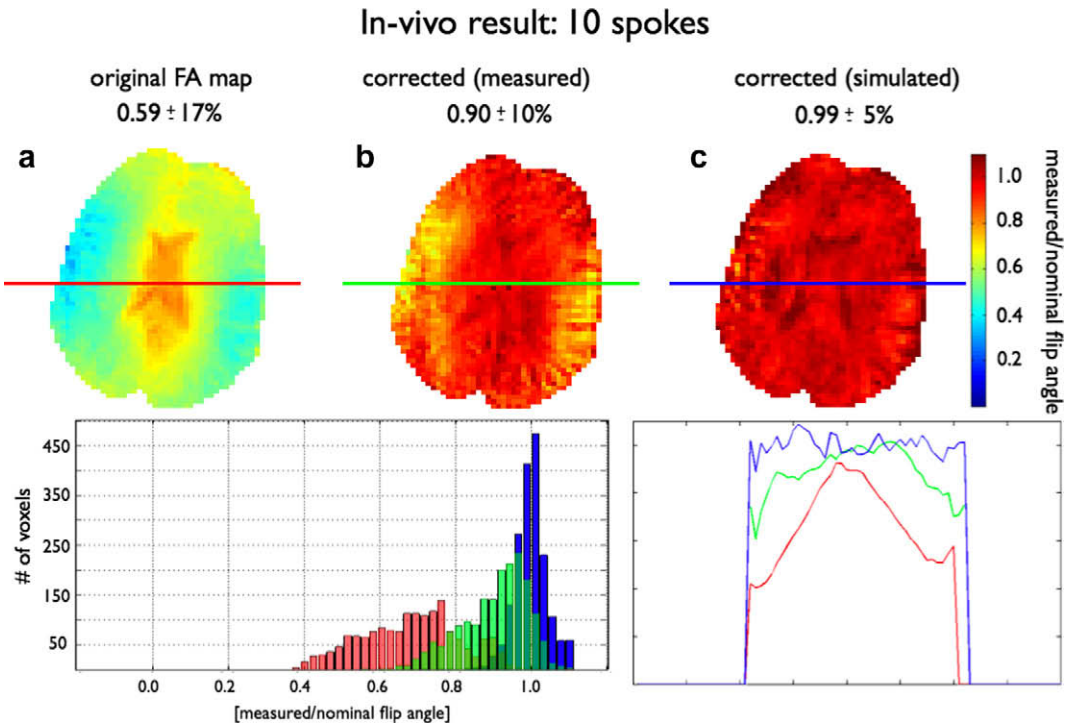

Fig. 16. Comparison between inhomogeneous flip-angle map (a) and a corrected map (b) based on a 10-spokes pulse. Additionally, a simulated result is shown (c). The histogram shows the distributions of the flip-angles for all the maps. Red, green and blue colors correspond to original, measured and simulated results, respectively. Both the histograms and profile lines show a visible discrepancy between simulation and experiment in low signal-to-noise ratio regions. (For interpretation of the references to color in this figure legend, the reader is referred to the web version of this paper.)

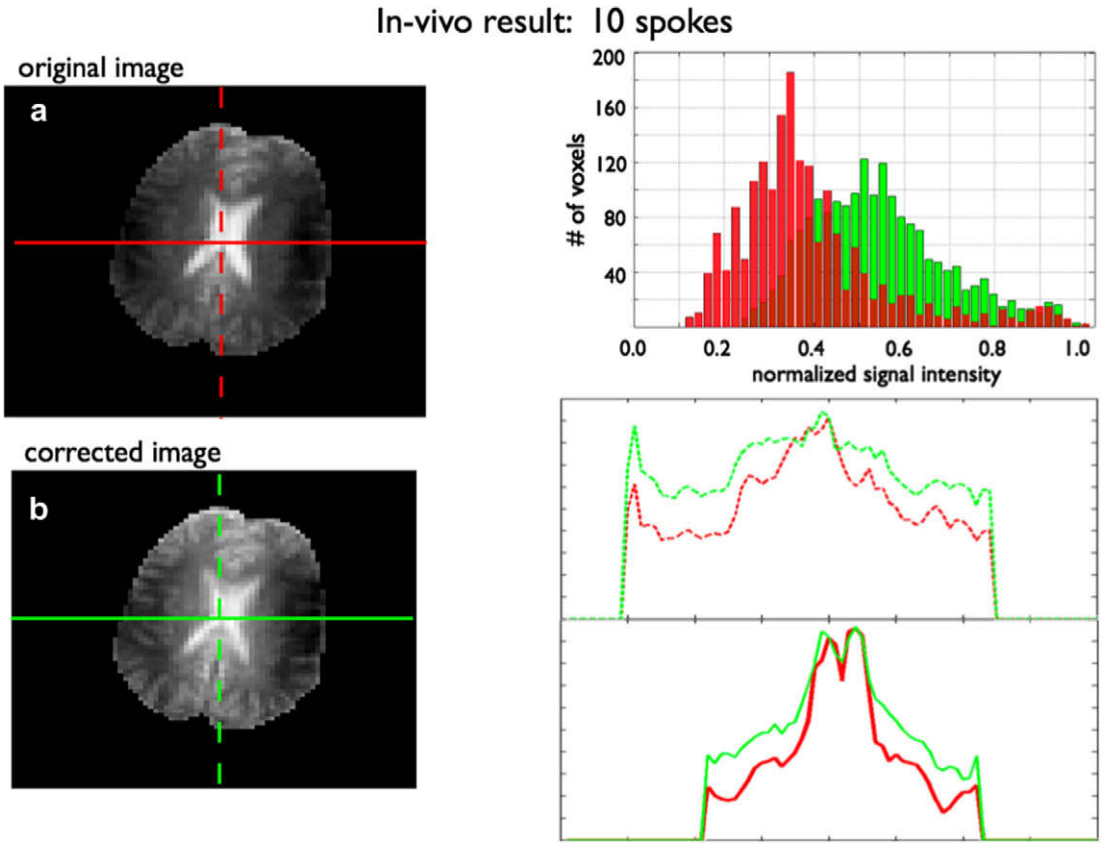

Fig. 17. Proton-density-weighted images, before (red) and after correction (green). The histogram shows overall improvement in relative intensity. The profile lines are presented for comparison of the signal intensity before and after correction. Moderate improvement in image quality is due to the fact that the image is a function of both inhomogenous (uncorrected) $(B_1^+)^*$ and the homogenous (corrected) flip-angle map. (For interpretation of the references to color in this figure legend, the reader is referred to the web version of this paper.)

ations are most likely not caused by the RF phase errors. Accumulation of phase due to small frequency errors (Fig. 10(c)) over extended periods of time (e.g. 16 min) leads to significant total phase errors (Fig. 10(a and b)). We acknowledge the fact that both B_1^+ and total phase calibration methods presented here are not ideal for clinical studies. However since the goal of this study is focused more on the effects of RF phase errors on the performance of the sparse-spokes sequence, the B_1^+ fitting method was chosen for its accuracy, despite its poor time efficiency. Furthermore, we conclude that the measurement of the total phase accumulation over 16 min implies that it would be challenging to perform successful spokes experiments without the immediate prior acquisition of the subject's specific field maps.

The optimization routine that we use in the pulse design uses B_1^+ and total phase collected after each spoke as inputs. Both of these inputs are susceptible to noise and measurement uncertainty. We argued that total phase measurement instabilities together with the susceptibility of sparse-spoke pulses to RF noise and noise in high-frequency spatial B_1^+ maps, are to be blamed for the discrepancies between simulations and experiments in low signal-to-noise ratio regions, as presented in Fig. 17. Although more experimental studies are needed, these will benefit from different (faster) B_1^+ mapping methods [16,17]. Moreover, usage of higher EPI factors (i.e. higher than 3, used in this study) combined with parallel imaging (fewer spokes) would further decrease time needed for measurement of total phase maps. We performed simulations to test how the designed pulses perform when realistic experimental conditions were taken into account. A 10-spokes pulse outperforms a 5-spokes pulse as the latter one cannot mitigate RF non-uniformities as well as the former, even though they both have similar linear dependence on the induced RF noise. We also introduced a simple solution to the problem of T_2^* and saturation effects acting on the RF amplitudes of sub-pulses of long pulses with $n_{spokes} > 10$ (Fig. 14). The solution re-scales individual RF amplitudes to minimize the unwanted effects. We can be more quantitative in our analysis and explain this behavior in a more rigorous fashion. Namely, the longitudinal component M_z of the magnetization vector never fully recovers to the initial value M_0, i.e., after the first pulse was played out:

$$M_z^1 = M_z^0 \cos(\theta) + M_0[1 - \exp(-TR/T_1)] \tag{13}$$

However, due to the fact that the effective TE_i time, measured from the center of ith sub-pulse to the acquisition time, is getting shorter as we move from one spoke sub-pulse to the next one, the transverse magnetization, hence the NAI value, recovers. For example, after the first sub-pulse transverse magnetization is:

$$M_{tr}^1 = M_z^0 \sin(\theta) \exp\left(-TE_1/T_2^*\right) \tag{14}$$

Both M_z and M_{tr} are then given by an iterative relation as follows:

$$M_z^i = M_z^{i-1} \cos(\theta) + M_0[1 - \exp(-TR/T_1)] \tag{15}$$

$$M_{tr}^i = M_z^{i-1} \sin(\theta) \exp\left(-TE_i/T_2^*\right) \tag{16}$$

The pseudo-oscillatory behavior of NAI is due to eddy-currents induced by the oscillating G_z waveform, from the center of the imaged slice. It is also clear why these effects are not present in shorter pulses, the effective echo times for spokes in a short sequence are short enough that transverse magnetization does not have time to decay noticeably. The compensation of the sub-pulse amplitudes does not represent a solution to the problem of long pulses in the presence of T_2^* relaxation and saturation effects. It does, however,

mitigate these problems to some degree, and we believe the exploration of this potentially useful technique is worthwhile. We analyzed the performance of pulses obtained through the optimization of the modified minimization condition, described in Section 3.7 and found the resulting solution, although not optimal, is able to correct the inhomogeneity to 58% of the initial value.

In conclusion, approximated modulation patterns generated by sparse-spokes pulses, effectively correct the modulation profile so that the resulting flip-angle map is nearly homogenous, i.e., the deviations of the measured flip-angles from the nominal angle are less than $\pm 10\%$ in the human head. We found that there is a trade-off between the pulse length and performance. The longer pulses are more susceptible to RF errors, saturation and T_2^* relaxation effects. Short pulses are not able to reduce non-uniformities effectively, so a compromise has to be found. The pulse with only 10 spokes shows relatively good performance, and is robust in the presence of relaxation effects. RF field inhomogeneities are a major cause of poor image quality in 7 T and higher field systems. The design of new pulses optimized to achieve improved flip-angle homogeneity enhances image quality, improving and expanding the diagnostic capabilities of ultra-high field MRI, and will complement other approaches to overcoming RF non-uniformity at high fields.

Acknowledgments

This work was supported by NIH grant number RO1EB000461.

References

[1] P. Van de Moortele et al., $\widehat{B}_1$ destructive interferences and spatial phase patterns at 7 T with a head transceiver array coil, MRM 54 (2005) 1503.
[2] S. Saekho et al., Fast-kz three-dimensional tailored radiofreq. pulse for reduced $\hat{B}_1$ inhom., MRM 55 (2006) 719.
[3] K. Setsompop et al., Sparse spokes slice selective design for $\hat{B}_1$ inhom. corrections at 7 T, Proc. Intl. Soc. Mag. Reson. Med. 15 (2007) 256.
[4] K. Setsompop et al., Slice-selective RF pulses for in vivo B_1^+ inhomogeneity mitigation at 7 T using parallel RF excitation with a 16-element coil, MRM 60 (2008) 1422.
[5] K. Setsompop et al., High-flip-angle slice selective parallel RF transmission with 8 channels at 7 T, J. Magn. Reson. 195 (2008) 76.
[6] D.I. Hoult, The principle of reciprocity in signal strength calculations a mathematical guide, CMR 12 (4) (2000) 173.
[7] J. Pauly, D. Nishimura, A. Macovski, A *k*-space analysis of small-tip-angle excitation, J. Magn. Reson. 81 (1989) 43.
[8] H. Yan, B. Chen, J.C. Gore, Approximate solutions of the Bloch equations for selective excitation, J. Magn. Reson. 75 (1987).
[9] T.S. Ibrahim et al., Effect of RF coil excitation on field inhomogeneity at ultra high fields: afield optimized TEM resonator, MRM 19 (2001) 1339.
[10] R. Stollberger, P. Wach, Imaging of the active B_1 field in vivo, Magn. Reson. Med. 35 (1996) 246–251.
[11] V.L. Yarnykh, Actual flip-angle imaging in the pulsed steady state: a method for rapid three-dimensional mapping of the transmitted radiofrequency field, Magn. Reson. Med. 57 (2007) 192.
[12] V.L. Yarnykh, Optimal spoiling of the transverse magnetization in the actual flip-angle imaging (AFI) sequence for fast B_1 field mapping, Proc. Intl. Soc. Mag. Reson. Med. 16 (2008).
[13] A.C. Zelinski et al., Fast slice-selective radio-frequency excitation pulses for mitigating $\hat{B}_1^+$ inhomogeneity in the human brain at 7 T, MRM 59 (2008) 1355.
[14] J.E. Moore, M. Jankiewicz, H. Zeng, A.W. Anderson, M.J. Avison, E.B. Welch, J.C. Gore, Quantitative comparison of B_1^+ mapping methods for 7 T human imaging, Proc. Intl. Soc. Mag. Reson. Med. 17 (2009) 372.
[15] A.M. Peters et al., T_2^* measurements in human brain at 1.5, 3 and 7 T, MRI 25 (2007) 748.
[16] A.B. Kerr et al., Accelerated B1 mapping for parallel excitation, Proc. Intl. Soc. Mag. Reson. Med. 15 (2007) 352.
[17] D.O. Brunner et al., Fast mapping of highly inhomogenous RF fields, Proc. Intl. Soc. Mag. Reson. Med. 15 (2007) 353.